HHS Public Access

Author manuscript

Sci Transl Med. Author manuscript; available in PMC 2016 November 11.

Published in final edited form as:

Sci Transl Med. 2015 November 11; 7(313): 313ra181. doi:10.1126/scitranslmed.aac8577.

Modeling pulmonary alveolar microlithiasis by epithelial deletion of the Npt2b sodium phosphate cotransporter reveals putative biomarkers and strategies for treatment

Atsushi Saito[1,*,†], **Nikolaos M. Nikolaidis**[1,*], **Hassane Amlal**[2], **Yasuaki Uehara**[1], **Jason C. Gardner**[1], **Kathleen LaSance**[3], **Lori B. Pitstick**[1], **James P. Bridges**[4], **Kathryn A. Wikenheiser-Brokamp**[5], **Dennis W. McGraw**[1], **Jason C. Woods**[6], **Yves Sabbagh**[7], **Susan C. Schiavi**[7], **Göksel Altinişik**[8], **Marko Jakopović**[9], **Yoshikazu Inoue**[10], and **Francis X. McCormack**[1,‡]

[1]Division of Pulmonary, Critical Care and Sleep Medicine, Department of Internal Medicine, The University of Cincinnati, Cincinnati, OH 45267, USA

[2]Department of Internal Medicine, University of Cincinnati, Cincinnati, OH 45267, USA

[3]Vontz Core Imaging Laboratory, Vontz Center for Molecular Studies, The University of Cincinnati, Cincinnati, OH 45267, USA

[4]Perinatal Institute, Division of Pulmonary Biology, Cincinnati Children's Hospital Medical Center, Cincinnati, OH 45229, USA

[5]Pathology and Laboratory Medicine, Cincinnati Children's Hospital Medical Center, Cincinnati, OH 45229, USA

[6]Pulmonary Imaging Research Center, Cincinnati Children's Hospital Medical Center, Cincinnati, OH 45229, USA

[7]The Sanofi-Genzyme R&D Center, Genzyme, a Sanofi company, Framingham, MA 01701, USA

[8]Department of Chest Diseases, Faculty of Medicine, Pamukkale University, Denizli 20160, Turkey

[9]Department for Respiratory Diseases, University Hospital Centre Zagreb, University of Zagreb School of Medicine, 10000 Zagreb, Croatia

[‡]Corresponding author. frank.mccormack@uc.edu.

[*]These authors contributed equally to this work.

[†]Present address: Departments of Biochemistry and Respiratory Medicine and Allergology, Sapporo Medical University School of Medicine, Sapporo 0608556, Japan.

Author contributions: F.X.M. developed the concept, and F.X.M., A.S., and N.M.N. designed the experiments, interpreted the data, and wrote the manuscript. A.S. and N.M.N. conducted the experimental work with help from H.A. for phosphate transport experiments, K.L. for radiological experiments, J.P.B. for phospholipid pool size experiments, K.A.W.-B. for pathological assessments, D.W.M. and L.B.P. for pulmonary physiological experiments, J.C.W. for radiological assessments, Y.U. for PTH and FGF-23 experiments, J.C.G. for statistical analysis, and Y.S. and S.C.S. for developing the Npt2b floxed mice. G.A., M.J., and Y.I. contributed to serum collection from PAM patients and discussion.

Competing interests: Y.S. and S.C.S. are employees of Genzyme, a Sanofi company, and own Sanofi stock. All other authors declare that they have no competing interests.

SUPPLEMENTARY MATERIALS

www.sciencetranslationalmedicine.org/cgi/content/full/7/313/313ra181/DC1)

[10]Department of Diffuse Lung Diseases and Respiratory Failure, Clinical Research Center, National Hospital Organization Kinki-Chuo Chest Medical Center, Osaka 5918555, Japan

Abstract

Pulmonary alveolar microlithiasis (PAM) is a rare, autosomal recessive lung disorder associated with progressive accumulation of calcium phosphate microliths. Inactivating mutations in SLC34A2, which encodes the NPT2b sodium-dependent phosphate cotransporter, has been proposed as a cause of PAM. We show that epithelial deletion of Npt2b in mice results in a progressive pulmonary process characterized by diffuse alveolar microlith accumulation, radiographic opacification, restrictive physiology, inflammation, fibrosis, and an unexpected alveolar phospholipidosis. Cytokine and surfactant protein elevations in the alveolar lavage and serum of PAM mice and confirmed in serum from PAM patients identify serum MCP-1 (monocyte chemotactic protein 1) and SP-D (surfactant protein D) as potential biomarkers. Microliths introduced by adoptive transfer into the lungs of wild-type mice produce marked macrophagerich inflammation and elevation of serum MCP-1 that peaks at 1 week and resolves at 1 month, concomitant with clearance of stones. Microliths isolated by bronchoalveolar lavage readily dissolve in EDTA, and therapeutic whole-lung EDTA lavage reduces the burden of stones in the lungs. A low-phosphate diet prevents microlith formation in young animals and reduces lung injury on the basis of reduction in serum SP-D. The burden of pulmonary calcium deposits in established PAM is also diminished within 4 weeks by a low-phosphate diet challenge. These data support a causative role for Npt2b in the pathogenesis of PAM and the use of the PAM mouse model as a preclinical platform for the development of biomarkers and therapeutic strategies.

INTRODUCTION

Pulmonary alveolar microlithiasis (PAM) is a rare, autosomal recessive lung disease in which calcium phosphate crystal formation in the alveolar space results in progressive radiographic opacification, pulmonary fibrosis, and respiratory failure (1–10). PAM is associated with consanguinity and is most common in Japan, Turkey, and Italy, with about 700 cases reported in the medical literature to date. Homozygosity mapping in patients with PAM was used to identify mutations in the *SLC34A2* gene, which encodes the type II sodium-dependent phosphate cotransporter NPT2b (11–14). *SLC34A2* was noted by in situ hybridization to be expressed in alveolar epithelial type II cells (AECII), and sodium-dependent phosphate transport was conferred upon oocytes by injection of wild-type RNA encoding Npt2b but not RNA containing Npt2b with naturally occurring mutations found in study subjects (15). These data provided strong circumstantial evidence that Npt2b expressed on AECII plays an important role in the regulation of phosphate homeostasis in the alveolar space (16). Other candidate sodium phosphate cotransporters that may be involved in alveolar phosphate transport include NPT2a, NPT2c, PIT1, and PIT2, encoded by the *SLC34A1*, *SLC34A3*, *SLC20A1*, and *SLC20A2* genes, respectively (17–19). In extrapulmonary organs, Npt2a and Npt2c are expressed mainly in the kidney and function to regulate urinary phosphate excretion (20, 21), whereas Npt2b is expressed primarily in the intestinal tract, where it plays an important role in the absorption of nutritional phosphate (22–27). In addition to the lung and gut, Npt2b is also expressed in the mammary gland, the

kidney, skin, prostate, and testes. Pit1 and Pit2 are ubiquitously expressed and play a key role in regulating intracellular phosphate levels (28). The goal of this study was to validate the role of Npt2b in the pathogenesis of PAM and to develop a tractable preclinical PAM model that could be interrogated for insights into disease mechanisms and used as a platform for development of biomarkers and treatment strategies.

RESULTS

Lung epithelium–specific deletion of Npt2b results in loss of sodium-dependent phosphate transport in isolated AECII

An epithelium-targeted Npt2b$^{-/-}$ mouse model was developed by breeding mice homozygous for floxed *Slc34a2* (22) with mice expressing Cre recombinase under the influence of the sonic hedgehog (*Shh*) promoter. The *Shh* promoter is active during development in epithelial tissues and has been used extensively as a tool to drive gene expression and deletion in the pulmonary epithelium (29, 30). Litter size was normal, gender distribution of the progeny was balanced, and pups appeared healthy with the expected Mendelian patterns of gene transmission of Cre and Npt2b floxed genes. Analysis of RNA from whole lung and isolated AECII from the Npt2b$^{-/-}$ mice by real-time polymerase chain reaction (rtPCR) revealed a marked decrease in *Slc34a2* message expression compared to Npt2b$^{+/+}$ mice and absence of compensatory up-regulation of sodium phosphate cotransporters *Slc34a1*, *Slc34a3*, *Slc20a1*, or *Slc20a2* (Fig. 1A). Immunostaining of lung sections revealed that Npt2b expression was restricted to AECII (identified by co-staining with anti-pro SP-C) in Npt2b$^{+/+}$ mice and was absent in lung tissues from the Npt2b$^{-/-}$ mice (Fig. 1B). The whisker-like pattern of staining on the luminal AECII surface was consistent with localization of Npt2b to the apical plasma membrane (Fig. 1B, arrows). Immunocytochemistry and immunoblotting of isolated AECII with anti-Npt2b confirmed expression of Npt2b exclusively in the pneumocytes derived from the Npt2b$^{+/+}$ mice but not Npt2b$^{-/-}$ littermates (Fig. 1, B to D). Sodium-dependent [^{32}P] phosphate transport was readily demonstrated in AECII isolated from Npt2b$^{+/+}$ mice but was absent in the AECII from Npt2b$^{-/-}$ mice (Fig. 1E) (31, 32).

To determine the effects of Npt2b deletion on the expression of sodium phosphate cotransporters in other organs, a gene expression survey of *Slc34a1*, *Slc34a2*, *Slc34a3*, *Slc20a1*, or *Slc20a2* in the lung, kidney, and ileum was performed in Npt2b$^{-/-}$ and Npt2b$^{+/+}$ mice (Fig. 1A and fig. S1). Npt2b was the major transporter expressed in the lung and ileum, whereas Npt2a and Npt2c predominated in the kidney. Pit1 and Pit2 were expressed in all tissues tested. In the Npt2b$^{-/-}$ mouse, Npt2b expression was very low to absent in the lung, and there was no obvious evidence of compensatory up-regulation of other sodium phosphate cotransporters.

There were no significant differences in serum electrolytes, hemoglobin, carbon dioxide, or glucose levels between Npt2b$^{+/+}$ and Npt2b$^{-/-}$ mice (table S1). No extrapulmonary manifestations or enhanced mortality was noted in the Npt2b$^{-/-}$ mice, although ruffled fur and immobility suggesting respiratory distress occasionally occurred in aged animals.

Deletion of the Npt2b transporter in lung epithelium alters alveolar homeostasis

There was marked elevation of both calcium and phosphate in the bronchoalveolar lavage (BAL) fluid (BALF) of the Npt2b$^{-/-}$ mice relative to the Npt2b$^{+/+}$ mice, but serum levels of both ions were nearly identical between the groups (Fig. 2A) (21). Early fractions from serial BAL of the Npt2b-deficient mouse revealed an opalescent and foamy appearance, consistent with the presence of surfactant material, and examination of total protein and surfactant protein D (SP-D) revealed elevated levels in the BALF (Fig. 2B). Saturated phosphatidylcholine (Sat PC) was also markedly increased in both BALF and homogenized lung tissue (LH) of the Npt2b$^{-/-}$ animals (Fig. 2C). Cytokine profiling of inflammatory mediators in BALF including MCP-1, MIP1β (macrophage inflammatory protein 1β), M-CSF (macrophage colony-stimulating factor), IP10 (interferon-γ–induced protein 10), VEGF (vascular endothelial growth factor), TNFα (tumor necrosis factor–α), and KC was used to select candidates for further testing in serum (Fig. 2D) (33). Serum SP-D and MCP-1 were elevated in Npt2b$^{-/-}$ animals compared to controls and increased with age in a manner that correlated with progressive microlith deposition (Fig. 2, E and F). Serum obtained from patients with PAM also revealed elevation of serum SP-D and MCP-1 compared to healthy volunteers (Fig. 2, G and H).

Dysregulation of phosphate transport in the lung results in progressive pulmonary alveolar microlith accumulation, marked inflammation, mild fibrosis, and restrictive lung physiology

Diffuse, hyperdense opacification was apparent on plain radiographs of the Npt2b$^{-/-}$ mice compared to Npt2b$^{+/+}$ littermates (Fig. 3, A and B). Micro–computed tomography (microCT) images of the chest showed dense ground-glass infiltrates, reticular and micronodular calcific opacities, and high density consolidation with air bronchograms (Fig. 3C). Although profusion of radiographic opacities on chest radiographs and CTs varied somewhat between Npt2b$^{-/-}$ mice of the same litter, longitudinal analysis of radiographic opacities by radiograph and CT revealed a consistent and progressive increase in infiltrates (Fig. 3D and fig. S2). Wet lung and ashed lung weights normalized to body weights of Npt2b$^{-/-}$ mice were consistently greater than those of Npt2b$^{+/+}$ mice starting as early as 4 weeks of age and progressively increased through time, as assessed at ages 4, 13, and 20 weeks (Fig. 3, E and F). Gender-associated differences in age-dependent radiographic opacification were not appreciated. von Kossa staining revealed accumulation of microliths in the alveolar spaces (Fig. 3G). Macrophage-rich inflammation and alveolar septal expansion were apparent in the lungs of Npt2b$^{-/-}$ mice, and in some regions was associated mild fibrotic change on trichrome staining (Fig. 3G). Foamy macrophages were abundant within inflammatory lesions, and macrophages isolated by BAL revealed punctate cytoplasmic Oil Red O staining consistent with accumulation of neutral triglycerides and lipids (Fig. 3H). The pressure volume curve of intubated and anesthetized Npt2b$^{-/-}$ mice was shifted down and to the right relative to Npt2b$^{+/+}$ animals, consistent with a restrictive physiologic defect, and the mean specific static compliance of 17-week-old Npt2b$^{-/-}$ mice was less than 50% of age-matched Npt2b$^{+/+}$ controls (Fig. 3I).

Adoptive transfer of alveolar microliths into Npt2b$^{+/+}$ lung results in transient macrophage-rich inflammation

To explore the direct inflammatory effects of microliths in the lung, and the potential for reversibility of lung lesions, we instilled calcium phosphate crystals isolated from Npt2b$^{-/-}$ mice into the lungs of Npt2b$^{+/+}$ mice by the intratracheal route. At 1 day after instillation, microliths were readily demonstrated in peribronchiolar air spaces by von Kossa staining of lung sections and by microCT, and although little or no inflammation was apparent by H&E staining, the microCT demonstrated areas of airspace opacity and consolidation consistent with edema or atelectasis (Fig. 4, A and B). By 7 days after instillation, intense macrophage-rich inflammation was present in peribronchiolar areas where stones were abundant, areas of consolidation persisted on microCT (Fig. 4A), and foci of collagen deposition and fibrosis were apparent by trichrome staining (Fig. 4B). One month after microliths were instilled, inflammation, fibrosis, and radiographic airspace opacities had largely resolved, and microliths were not detected by von Kossa staining (Fig. 4, A and B). Changes in serum MCP-1 levels closely paralleled the radiographic and histologic course after adoptive microlith transfer, more than tripling from baseline to peak inflammation at 7 days, and returning to near baseline at 1 month (Fig. 4C). The mean serum MCP-1 level of 16-week-old Npt2b$^{-/-}$ mice is shown for comparison.

Therapeutic lavage reduces pulmonary opacities and microlith burden

Infrared spectroscopy revealed that alveolar microliths isolated from Npt2b$^{-/-}$ mice were composed of calcium phosphate, predominantly hydroxyapatite. Microliths were observed to readily dissolve in buffers containing concentrations of EDTA or EGTA of 20 mM or greater (Fig. 5A). Lesser degrees of dissolution also occurred upon exposure to solutions with lower EDTA or EGTA levels, low-pH buffers, citrate, or high concentrations of etidronate (a bisphosphonate that inhibits calcium phosphate crystal formation). To explore the potential for therapeutic EDTA lavage to reduce the burden of microliths in the lung, we performed serial therapeutic alveolar lavage of euthanized Npt2b$^{-/-}$ mice with 1-ml aliquots of 20 mM Hepes-buffered saline alone or containing variable concentrations of EDTA (Fig. 5B). MicroCT and histologic analysis of the lungs before and after serial lavage revealed a reduction in calcific opacities when the chelating agent was present but not with saline alone. Clearance of stones appeared to be more effective with lavage fluid containing 500 mM EDTA than with 50 mM EDTA. The diameter of residual crystals on post-lavage lung histology also decreased in an EDTA concentration-dependent manner (Fig. 5, C to E, and fig. S3). The recovered lavage fluid was foamy and opalescent in the first seven or eight tubes, consistent with excess surfactant content, but became clearer with subsequent cycles (Fig. 5F). Pelleted microliths were present in tubes 1 to 7, indicating that the abundance of stones exceeded the chelating capacity of the EDTA solution early in the lavage series.

A low-phosphate diet attenuates the accumulation of microliths in the alveolar space

To determine the effect of reducing dietary phosphate intake on microlith formation, we fed 4-week-old Npt2b$^{-/-}$ mice a regular diet (RD) or a low-phosphate diet (LPD) for a total of 8 weeks. The pre- and postintervention microCT and von Kossa staining of lung sections revealed that LPD reduced the burden of microliths in the alveolar spaces (Fig. 6, A and B).

Wet lung weight normalized to body weight from the LPD group was also less than that of RD group (Fig. 6C). Although serum phosphate concentration and MCP-1 from the RD group were not different from LPD group, there was a trend toward lower values for each in the LPD mice (Fig. 6, D and F). Serum SP-D was lower in the LPD than in the RD group, consistent with improved maintenance of pulmonary epithelial barrier integrity in the LPD group (Fig. 6E). Fibroblast growth factor 23 (FGF-23), a cytokine that regulates the expression of sodium phosphate cotransporters Npt2a and Npt2c (22) to maintain phosphate homeostasis, was predictably decreased in LPD-treated Npt2b$^{+/+}$ and Npt2b$^{-/-}$ mice (Fig. 6G). Parathyroid hormone (PTH) was also lower in LPD than in the RD group for both mouse genotypes (Fig. 6G). rtPCR analysis of AECll from LPD-treated Npt2b$^{-/-}$ mice revealed a minor increase in Slc20a1 message expression compared to Npt2b$^{-/-}$ mice fed with RD. (Fig. 6I). To evaluate the potential for a dietary intervention to affect the microlith burden in aged Npt2b$^{-/-}$ mice with well-established pathological changes in the lung, we also treated 25- to 28-week-old mice with LPD for a period of 4 weeks. MicroCT before and after LPD challenge revealed a reduction in the burden of stones (Fig. 6J), which contrasted with the radiographic progression that occurred in Npt2b$^{-/-}$ mice challenged with RD.

DISCUSSION

Human genetic studies strongly implicated mutations in the *SLC34A2* gene in the pathogenesis of PAM (11, 12), but a direct causal role for the encoded sodium phosphate cotransporter, Npt2b, in alveolar phosphate homeostasis and microlith formation has not been demonstrated. To analyze the role of inactivation of Npt2b as an essential driver of PAM pathology, we crossed mice expressing a floxed allele for Npt2b with transgenic mice expressing Cre recombinase under the control of the sonic hedgehog promoter to enforce deletion of the transporter in the epithelial tissues (29, 30). Pathologic analyses revealed abnormalities only in the lungs. By 4 weeks of age, lamellar concretions were found in the alveolar spaces of all Npt2b$^{-/-}$ animals examined, but not in the control littermates. Infrared spectroscopy and von Kossa staining demonstrated that the microliths were composed of calcium phosphate. Macrophage-rich alveolar inflammation was also present, with elevations in a number of alveolar and serum cytokines, including MCP-1 (Figs. 2, D and F, and 3G). The accumulation of microliths in lung tissues progressed with time and became more widespread, chest radiographs and microCTs revealed progressive hyperdense opacification, and early, mild fibrosis and a restrictive physiologic defect developed (Fig. 3 and fig. S2). An unexpected alveolar phospholipidosis was present, including elevation in Sat PC and SP-D in BALF (Fig. 2, B and C). Adoptive transfer of microliths isolated from Npt2b$^{-/-}$ mice into the lungs of naïve wild-type mice resulted in intense acute peribronchiolar inflammation, dense radiographic opacities, and elevation of serum MCP-1, all of which peaked in 1 week and resolved in 28 days, in association with near-complete disappearance of microliths (Fig. 4, A to C). This result demonstrating the capacity of the normal lung to clear calcium phosphate microliths bodes well for therapeutic strategies targeting restoration of phosphate homeostasis, including gene correction approaches. The observation that microliths dissolved in EDTA suggested that therapeutic lavage with chelating agents might be an effective treatment strategy, and exhaustive intrapulmonary instillation and aspiration of a buffer containing 50 or 500 mM EDTA reduced the burden of

alveolar microliths postmortem (Fig. 5, A to F, and fig. S3). Finally, an LPD had a marked effect of calcium deposition and inflammation in the lung, in both young mice with nascent microlith formation and aged animals with established pathological changes. Collectively, these data demonstrate that loss of Npt2b function in the lung is necessary and sufficient for the development of PAM, that SP-D and MCP-1 are promising biomarkers of lung injury and disease progression, and that therapeutic lavage and dietary interventions are plausible therapeutic interventions for the treatment of PAM.

Our results demonstrate that the expression of Npt2b in the murine lung is restricted to the apical membrane of AECII and that targeted deletion of the transporter abolishes AECII sodium-dependent phosphate import (Fig. 1, B and E). Phosphate transporters Pit1 and/or Pit2 are also expressed in the pulmonary epithelium (fig. S1), but their subcellular localization and orientation in the plasma membrane are unknown, and they are clearly not able to compensate for loss of Npt2b under normal dietary conditions. The data are consistent with a model in which $Npt2b^{-/-}$ is the primary channel responsible for sodium-dependent transport of phosphate from the alveolar lumen across the apical plasma membrane into AECII (34). The transporters responsible for export of phosphate from AECII into serum have not been explored, but Pit1 and/or Pit2 are good candidates based on their localization to the basolateral cell membrane in other organs. We found no evidence for compensatory up-regulation of other sodium phosphate co-transporters, including Npt2a, Npt2c, Pit1, or Pit2 in the $Npt2b^{-/-}$ mice on a diet with normal levels of dietary phosphate (Fig. 1A and fig. S1), but type l sodium phosphate transporters (*Slc17* family) (35) and other phosphate channels have not yet been examined. On an LPD, *Slc20a1* expression was slightly elevated in AECll (Fig. 6I), suggesting the possibility that up-regulation of *Slc20a1* played a role in the reduction of the burden of microliths.

The loss of Npt2b resulted in an increase in the levels of phosphate in the alveolar lining fluid, accompanied by an increase in alveolar calcium concentration (Fig. 2A). The latter is unexplained but may be a mechanism to maintain electroneutrality. Elevations in the calcium phosphate index are associated with hydroxyapatite crystal formation (36). We propose that the phosphate in the alveolar space of $Npt2b^{-/-}$ mice is liberated by alveolar macrophages in theprocess of surfactant catabolism and accumulates because transport into AECII and subsequent passive or active transport across the basolateral membrane into the serum are defective (37).

We were surprised to find that deletion of the Npt2b transporter resulted in an alveolar phospholipidosis, including a marked elevation in Sat PC and SP-D in BAL (Fig. 2, B and C). Disruption in surfactant homeostasis has not been reported in patients with PAM, although lipid-laden macrophages that stain with Oil Red O have been described (38), as have elevations in serum surfactant proteins (39). At this time, it is not clear whether the mechanism of surfactant accumulation in the $Npt2b^{-/-}$ mice is related to an increase in surfactant synthesis or altered catabolism, although it seems likely that decreased surfactant degradation by dysfunctional alveolar macrophages engorged with microliths may play a role (40). It is also possible that alveolar phosphate levels or the Npt2b transporter directly influences surfactant synthesis or catabolism. The elevation in serum SP-D in PAM mice could reflect increased translocation across the alveolar basement membrane driven by

higher alveolar SP-D levels or compromised barrier integrity or both. We confirmed that SP-D was elevated in the serum of patients with PAM, as originally described in two patients by Takahashi *et al*. (39), but did not find significant elevations of serum SP-A as reported by that group. Small patient numbers and variation in disease severity certainly contribute to these differences between groups.

Intense macrophage predominant alveolar inflammation developed in the Npt2b$^{-/-}$ mice, associated with multifocal consolidated lesions, giant cells containing intracytoplasmic inclusions (Fig. 3G), and marked elevations in alveolar cytokines and chemokines that influence macrophage function. Scattered areas of collagen deposition and a restrictive physiologic defect developed. The reduced lung compliance was almost certainly attributable to inflammation because the fibrosis seen on the lung sections was quite mild. Several cytokines were also increased in the serum of Npt2b$^{-/-}$ mice, including MCP-1, suggesting possible utility as biomarkers (Fig. 2F). Consistent with this notion, elevated serum MCP-1 was also identified in serum obtained from patients with PAM (Fig. 2H), which has not been reported previously. Adoptive transfer of microliths into the lungs of wild-type mice produced a transient, intense peribronchiolar inflammation and serum MCP-1 elevation peaking at 1 week, demonstrating that microliths are sufficient to reproduce the inflammatory phenotype of the Npt2b$^{-/-}$ mice in the absence of dysregulated alveolar phosphate homeostasis (Fig. 4, A to C). The observation that the lesions were also completely resolved within 1 month after instillation indicates that alveolar macrophages have the potential to degrade microliths and that therapies targeted at restoring phosphate homeostasis have the potential to reverse some of the pathological manifestations of PAM. In addition, the finding that serum MCP-1 level tracks with the development and resolution of alveolar inflammation suggests the possibility that MCP-1 may be useful as a biomarker of disease activity.

Microliths isolated from the Npt2b$^{-/-}$ mice readily dissolved in EDTA and EGTA, suggesting a plausible treatment strategy. Serial lavage of the lungs of sacrificed mice resulted in a marked reduction in the burden of microliths, based on radiographic and histological examination (Fig. 5, A to F, and fig. S3). EDTA is an excipient in many respiratory inhalers and has been delivered at 100 mM concentration without an apparent safety signal in a nebulized therapy trial to children with cystic fibrosis (41), but the toxicity of EDTA or EGTA as a component of therapeutic lavage fluid has not been tested (42, 43). We were surprised to find that dietary phosphate restriction produced a marked reduction of stone burden and lung weight despite the maintenance of near-normal serum phosphate levels (Fig. 6, A to D). Reduction in the level of serum SP-D suggests that LPD preserves pulmonary epithelial barrier integrity (Fig. 6E). LPD also reduced the burden of microliths in aged Npt2b$^{-/-}$ mice with established PAM pathology, suggesting the possibility that a simple dietary intervention in PAM patients may partially reverse lung pathological changes in those with advanced disease (Fig. 6J). Although the up-regulation of *Slc20a1* is an intriguing finding that may play a role in the benefit of LPD on microlith burden, the magnitude of this effect is small, and further studies will be required. On the basis of these preclinical observations, pilot studies of limited, therapeutic EDTA lavage and/or LPD in patients with PAM may be worthy of consideration.

In summary, deletion of Npt2b from the pulmonary epithelium of mice recapitulates PAM in humans, including alveolar microlith formation, diffuse radiographic opacity, macrophage-rich inflammation, and a restrictive ventilatory defect. The development of alveolar phospholipidosis suggests a previously unappreciated role for the Npt2b transepithelial phosphate transporter in surfactant homeostasis. The finding that lungs with intact Npt2b-dependent phosphate transport have the capacity to clear microliths suggests that correction of transepithelial phosphate transport may be sufficient to prevent and possibly reverse disease progression. Therapeutic EDTA lavage and reduction of dietary phosphate intake are promising strategies for human trials. We conclude that the PAM mouse model is an excellent platform for exploring PAM disease pathogenesis, identifying novel biomarkers and mechanisms regulating alveolar homeostasis, and testing genetic, interventional, and pharmaceutical therapeutic approaches.

MATERIALS AND METHODS

Study design

The purpose of this study was to develop a preclinical mouse model to better understand the pathogenesis of PAM, discover biomarkers, and develop approaches to treatment. Our initial hypothesis was that epithelium-specific deletion of Npt2b defect would recapitulate PAM in mice, including microlith accumulation, alveolar inflammation, pulmonary fibrosis, and respiratory failure. This hypothesis was proven true for all but the last two features. The primary end points were radiographic density, wet and ashed lung weights, qualitative histologic and immunohistochemical assessments, lung compliance, and inflammatory cytokine levels in lavage fluid, lung tissue, and serum. To identify biomarkers of potential relevance to humans, measurement of MCP-1 was conducted in serum of PAM patients. The unexpected finding that PAM mice develop a phospholipidosis in the tissue and alveolar lining fluid compartments led to a new hypothesis that phosphate homeostasis plays a role in surfactant synthesis, secretion, or degradation. The primary end points in these studies were phospholipid pool sizes in the tissue and alveolar compartments, and SP-D levels in serum and lavage of the Npt2b mice. To assess clinical utility, these serum SP-D studies were extended to human samples. Fully testing this hypothesis was beyond the scope of the current study and will be the subject of another article. The finding that microliths are cleared from the normal lung after adoptive transfer suggested that corrective strategies that restore normal Npt2b function have the potential to arrest or reverse microlith-induced inflammation. The primary end points for these studies were based on histological and inflammatory cytokine assessments. Fully testing this hypothesis was beyond the scope of the current study and will be the subject of another article. The observation that isolated microliths dissolve in EDTA solutions suggested the hypothesis that therapeutic EDTA lavage was a plausible therapeutic strategy for PAM. Secondarily, low dietary phosphate intake was shown to reduce the burden of microliths. The primary end point for these studies was the histological and radiographic assessment of microlith burden after living and postmortem lavage. Sample sizes were predetermined on the basis of statistical considerations and on pilot experiments that indicated the number of mice per group needed to generate statistical significance. For patients, our sample size was limited by the number of samples we were able to collect for this ultrarare disease. Outliers were not excluded from

analyses. Because of the markedly different phenotypes of the wild-type and Npt2b$^{-/-}$ animals, randomization and blinding were not used for experiments with animals, but mice were age- and sex-matched for all studies. Patients with a physician-rendered diagnosis of PAM and a compatible radiograph were identified through the Rare Lung Diseases Consortium (www.rarediseasesnetwork.org/cms/RLD). The experimental procedures were approved by the Institutional Animal Care and Use Committee at the University of Cincinnati.

Animals

Mice (129J background) containing flox P sites flanking exon 6 of the *Slc34a2* gene (Npt2b$^{fl/fl}$) developed by Genzyme for systemic phosphate homeostasis studies (22) were bred with sonic hedgehog Shh-Cre promoter–expressing mice (C57BL/6NTac background, The Jackson Laboratory) to drive epithelium-specific deletion of the Npt2b gene. The breeding strategy used was to cross Npt2b$^{fl/fl}$.Cre $^{+/-}$ with Npt2b$^{fl/fl}$.Cre $^{-/-}$ mice to generate equal numbers of Npt2b knockout animals, heterozygous animals (Npt2b$^{fl/fl}$.Cre $^{+/-}$), and littermate controls (Npt2b$^{fl/fl}$.Cre $^{-/-}$). Progeny were genotyped by PCR amplification of genomic DNA using PCR primers 5′-CTGGGATCAAA-TGGTCAGAGAG-3′ and 5′-GAGCACACGAACAAGTAGAGAA-3′. All animals were maintained in a specific pathogen–free facility and were handled according to the University of Cincinnati Institutional Animal Care and Use Committee–approved protocol and National Institutes of Health guidelines.

Antibodies

The anti-Npt2b antibody used was generated in rabbit as previously described (Genzyme) (22). Rabbit anti-pro SP-C antibody was purchased from Seven Hills Bioreagents.

MicroCT and x-ray imaging

After animals were anesthetized with isoflurane, two-dimensional (2D) chest x-ray images (In-Vivo Multispectral Imaging System FX, Bruker) were obtained, and microCT scans (Inveon, Siemens) were performed with respiratory gating applied during image acquisition to minimize breathing motion artifacts. The Inveon Research Workplace (Siemens) general analysis and 3D Visualization software were used for image review and analysis and to produce 3D volume-rendered images. For postmortem CT studies, mice were sacrificed by intraperitoneal injection of Fatal-Plus solution (Vortech), intratracheally intubated with a 20-gauge plastic catheter, and inflated with air to a pressure of 20 cm H_2O.

Histology

Mice were sacrificed and tissues were fixed with 10% buffered formalin phosphate, embedded in paraffin, and stained with H&E. The von Kossa staining technique was used to stain calcium deposits in the lung by application of 3% silver nitrate to the lung sections, exposure to strong light for 30 min, and counterstaining with Nuclear Fast Red 5 (Polysciences Inc.). Masson’s trichrome staining was used to identify collagen deposition (Newcomer Supply). Intracellular lipid deposits were identified by Oil Red O staining after

fixation with 10% buffered formalin, incubation in propylene glycol (Newcomer Supply), and counterstaining with hematoxylin (44).

Immunohistochemistry and immunocytochemistry

Tissue sections were incubated with anti-Npt2b antibodies at the indicated concentrations overnight at 4°C. After washing with tris-buffered saline containing 0.1% Tween 20, tissues were incubated with horseradish peroxidase (HRP)–labeled anti-rabbit goat secondary antibody (BA-1000, Vector Laboratories) for 1 hour at room temperature. The DAB substrate kit (Thermo Fisher) was used for color development, and samples were counterstained with hematoxylin. For immunocytochemistry, cells were cytospun onto glass slides, dried overnight, and stained with anti-Npt2b antibodies at various dilutions for 1 hour at 37°C. After incubation with HRP-labeled DyLight 488 affinity-purified donkey anti-rabbit immunoglobulin G (IgG) (Jackson ImmunoResearch) for 1 hour at 37°C, color development with DAB and counterstaining with DAPI were performed.

Isolation of AECII

Mice were sacrificed by intraperitoneal injection of Fatal-Plus solution (Vortech), and lungs were perfused with 10 ml of sterile normal saline via the pulmonary artery. The airway was cannulated via tracheostomy with a 20-gauge metallic angiocatheter, and 3 ml of dispase (50 caseinolytic units/ml, Corning) was instilled, followed by 0.5 ml of 1% low-melt agarose (warmed to 45°C). Lungs were rapidly cooled on ice for 2 min, incubated in 1 ml of dispase for 45 min at room temperature, and transferred to a culture dish containing deoxyribonuclease I (100 U/ml) (Worthington). The parenchymal lung tissue was gently teased from the bronchi and homogenized. Cell suspensions were filtered, collected by centrifugation, and placed on prewashed 100-mm tissue culture plates coated with CD45 and CD32/16 antibodies (BD Biosciences). After incubation for 60 min at 37°C in a 5% CO_2 atmosphere to promote adherence of contaminating macrophages and fibroblasts, the AECII were gently panned from the plate, collected by centrifugation, and counted. For the $Npt2b^{-/-}$ animals, differential centrifugation was used to separate microliths from the cells. Cell viability determined with trypan blue staining was routinely >90%, and cell purity determined by SP-C staining ranged from 75 to 90%.

Immunoblotting analysis

Isolated AECII were lysed in radioimmunoprecipitation assay buffer (Santa Cruz Biotechnology) with protease inhibitor cocktail (P8340, Sigma) on ice for 30 min, solubilized in reducing buffer, loaded into SDS-PAGE wells at equal protein concentrations, transferred to PVDF membrane (Immobilon-P, Millipore), and immunoblotted with anti-Npt2b antibody (1:1000 dilution). LI-COR IRDye goat anti-rabbit IgG was used as the secondary antibody. Protein species were visualized using the Odyssey Infrared Imaging System (LI-COR).

Serum and alveolar lining fluid collection and measurements

Mice were sacrificed using Fatal-Plus solution (Vortech) and lavaged with 1 ml of normal saline through a 20-gauge angiocatheter inserted into trachea. Phosphate was measured by

using Phosphate Colorimetric Assay Kit (BioVision) per the manufacturer's directions. Calcium levels were determined after dehydration of BALF and reconstitution in distilled H_2O using colorimetric methods according to the manufacturer's directions (BioVision). Total protein in BALF was measured by BCA Protein Assay Kit (Pierce), and mouse SP-A and mouse SP-D in the BALF were measured by ELISA according to previously published methods (45). Mouse SP-D in the serum was measured by a rat/mouse ELISA kit (YAMASA), and human SP-D was measured by Quantikine ELISA Kit (R&D Systems Inc.). MCP-1 in mouse serum was measured using the mouse CCL2 [chemokine (C-C motif) ligand]/JE/MCP-1 ELISA kit, and human CCL2/MCP-1 was measured with the ELISA kit, both from R&D Systems Inc. Luminex multiplex technology was used for cytokine array profiling on BALF as described previously (33). Sat PC in BALF and lung homogenates were quantified as previously described (46). Human sample collection and laboratory analysis were approved by the Institutional Review Board at The University of Cincinnati College of Medicine. Phosphate homeostasis hormones were measured in mouse serum using the FGF-23 ELISA Kit (Kainos Laboratories Inc.) and the Mouse PTH 1-84 ELISA Kit (Immutopics).

Phosphate transport measurement using [^{32}P] phosphate flux

Isolated AECII were washed twice by centrifugation (1 min, 50g, 4°C) and incubated for 10 min at 37°C in HCO_3^-- and Na^+-free solution containing 140 mM TMA chloride, 5 mM KCl, 1 mM $MgCl_2$, 0.1 mM K_2HPO_4, 1 mM $CaCl_2$, 10 mM Hepes, and 5 mM glucose adjusted to pH 7.40 with tris base. Cells were then exposed to either 140 mM TMA or 140 mM NaCl and 3 μCi of ^{32}P-labeled phosphoric acid (PerkinElmer) for 10 min at 37°C. Phosphate uptake was stopped by addition of 1 ml of ice-cold stop solution containing 140 mM NaCl, 1 mM $CaCl_2$, 10 mM Hepes, and 10 mM Na-arsenate (pH 7.40). The cell suspension was washed three times with the same ice-cold solution before adding lysis buffer (0.1 mM NaOH + 0.5% Triton X-100). The samples were then normalized on the basis of protein concentration determined using the Bio-Rad Protein Assay Kit before loading into a scintillation counter for counting.

Quantitative rtPCR

RNA from tissues of Npt2b$^{-/-}$ and Npt2b$^{+/+}$ mice was isolated using the RNeasy Micro Kit (Qiagen). After first-strand complementary DNA synthesis using SuperScript III Reverse Transcriptase (Invitrogen), quantitative rtPCR was performed with a SYBR Green Master Mix (Applied Biosystems) and primer pairs for sodium phosphate cotransporters, as well as β-*actin* as an internal control. The nucleotide sequences of the primer pairs were 5′-CACTACCACTACAGCCATCC-3′ and 5′-GATGCCCGAGATGTTGAAGA-3′ for *Slc34a1*, 5′-CTGGGAT-CAAATGGTCAGAGAG-3′ and 5′-GAGCACACGAACAAGTAGA-GAA-3′ for *Slc34a2*, 5′-CCTACTCTGGATGCCTTTGAC-3′ and 5′-CCATGCCAACCTCTTTCAGT-3′ for *Slc34a3*, 5′-GTGTCCCTTCTCTTCCAGTTC-3′ and 5′- TGTTGCCGCTTTTGTAGAG-3′ for *Slc20a1*, 5′-CCTGCTCTTCCACTTCCTG-3′ and 5′-TCTTGTGTAACTCCGCCTTG-3′ for *Slc20a2*, and 5′-ACCTTCTA-CAATGAGCTGCG-3′ and 5′-CTGGATGGCTACGTACATGG-3′ for β-*actin*.

Composition and solubility of crystals

Crystals isolated by BAL of Npt2b$^{-/-}$ mice were extensively washed with normal saline and analyzed by infrared spectroscopy to determine elemental composition (Gerald V. Ling Urinary Stone Analysis Laboratory). Solubility of isolated microliths was determined by suspension in 100 μl of 20 mM Hepes saline at varying pH and with varying concentrations of the chelating agent EDTA, EGTA, etidronate, or citrate. After vortexing for 30 s, the microlith mixtures were loaded into round-bottom plates (BD), centrifuged at 400*g* for 5 min, and visually inspected for evidence of dissolution.

Lung physiological measurements using Scireq flexiVent system

Mice were anesthetized with isoflurane or ketamine and intubated through a tracheotomy with a metallic angiocatheter. Lung compliance and pressure volume characteristics were measured using oscillatory impedance (flexiVent, version 5.1, Scireq Inc.) and plotted using GraphPad Prism (version 5.03, GraphPad Software Inc.) as previously reported (47).

Lung and ash weight

Wet and ashed lung weights were measured in mice of various ages and normalized to body weight. For ashing, lungs were cremated at 600°C in an oven for 10 min.

Adoptive transfer of microliths

Microliths were recovered from Npt2b$^{-/-}$ mice lungs during AECII isolation. Microliths were incubated with 1% Triton X-100 in normal saline and extensively washed and resuspended in Hepes-buffered saline. Equal quantities of isolated microliths (amounting to about 50% of the typical microlith burden of an 8-week-old Npt2b$^{-/-}$ mouse) in 100 μl of Hepes-buffered saline were intratracheally instilled into each Npt2b$^{+/+}$ mouse, followed by histologic and radiographic analyses at various time points.

Postmortem lavage with EDTA

Sacrificed Npt2b$^{-/-}$ mice were intubated via tracheostomy with a 20-gauge metallic angiocatheter, and after inflation of the lung to 20–cm H_2O pressure, scanned by microCT. Serial BALs (1 ml, 15 cycles) were performed with 20 mM Hepes saline containing the indicated concentrations of EDTA (pH 7.4). After the lavage, lung inflation and microCT of the chest were again performed. Recovered BALF from each instillation/aspiration cycle was centrifuged at 400g for 3 min and visually inspected.

Low-phosphate diet

Regular phosphate content chow and low-phosphate chow containing, respectively, 22.5%/16% protein, 42.7%/70% carbohydrate, 5.2%/5% fat, 1.2%/0.6% calcium, 1.0%/0.02% phosphate, and vitamin D (5100 IU kg^{-1}/2200 IU kg^{-1}) were purchased from Harlan. Recently weaned mice (3 or 4 weeks) were fed with RD or LPD for the indicated time intervals. MicroCT images were taken at the beginning and at the end of the study, together with wet lung and body weight measurement, and serum collection for biomarkers. Wet lung weight normalized to body weight was compared for mice fed with RD and LPD. In the rtPCR study, 4-week-old mice were fed with RD or LPD for 2 weeks. For experiments to

determine whether microlith accumulation can be reversed, 25- to 28-week-old mice were fed with LPD for 4 weeks, and pre- and post-microCT was performed.

Statistical analysis

All data are presented as means ± SD. Data from each experiment were confirmed by one or more replicate experiments. Most of our data did not meet the equality of variance assumption for the Student's *t* test, so an unpaired *t* test with the Welch correction was used for all statistical comparisons of two groups. In experiments where more than two groups were compared, an ANOVA and Bonferroni posttest comparing selected groups were used, and a $P < 0.05$ was considered to indicate statistical significance. These data were analyzed with GraphPad Prism (version 5.03, GraphPad software Inc.). All raw data and P values can be found in table S2.

Supplementary Material

Refer to Web version on PubMed Central for supplementary material.

Acknowledgments

We thank M. Kuro-o (Jichi Medical University, Shimotsuke, Toguichi, Japan) for sharing the Npt2b floxed mice. Also, we thank E. Kopras and G. Meyers from University of Cincinnati, Cincinnati, OH, for coordinating collection of samples from PAM patients. We thank L. James from Shriners Hospitals for Children, Cincinnati, OH, for statistical analysis.

Funding: This work was supported by HL127455 (to F.X.M.), the Carespring Foundation (to F.X.M.), and DK083582 (to H.A.). Patient samples were collected through the Rare Lung Disease Consortium (U54HL127672, Director-Bruce Trapnell, co-Director F.X.M.), part of Rare Diseases Clinical Research Network (RDCRN), an initiative of the Office of Rare Diseases Research (ORDR) and the National Center for Accelerating Translational Science (NCATS). The RLDC is funded through collaboration between NCATS and the National Heart Lung and Blood Institute (NHLBI).

REFERENCES AND NOTES

1. Ferreira Francisco FA, Pereira e Silva JL, Hochhegger B, Zanetti G, Marchiori E. Pulmonary alveolar microlithiasis. State-of-the-art review. Respir Med. 2013; 107:1–9. [PubMed: 23183116]
2. Gupta N, McCormack FX. Pulmonary alveolar microlithiasis. Am J Respir Crit Care Med. 2013; 188:e11–e12. [PubMed: 24083869]
3. Tachibana T, Hagiwara K, Johkoh T. Pulmonary alveolar microlithiasis: Review and management. Curr Opin Pulm Med. 2009; 15:486–490. [PubMed: 19617834]
4. Mariotta S, Ricci A, Papale M, De Clementi F, Sposato B, Guidi L, Mannino F. Pulmonary alveolar microlithiasis: Report on 576 cases published in the literature. Sarcoidosis Vasc Diffuse Lung Dis. 2004; 21:173–181. [PubMed: 15554073]
5. Whitsett JA, Wert SE, Weaver TE. Diseases of pulmonary surfactant homeostasis. Annu Rev Pathol. 2015; 10:371–393. [PubMed: 25621661]
6. Devine MS, Garcia CK. Genetic interstitial lung disease. Clin Chest Med. 2012; 33:95–110. [PubMed: 22365249]
7. Lauta VM. Pulmonary alveolar microlithiasis: An overview of clinical and pathological features together with possible therapies. Respir Med. 2003; 97:1081–1085. [PubMed: 14561014]
8. Castellana G, Lamorgese V. Pulmonary alveolar microlithiasis. World cases and review of the literature. Respiration. 2003; 70:549–555. [PubMed: 14665786]
9. Sahoo MK, Karunanithi S, Bal CS. Pulmonary alveolar microlithiasis: Imaging characteristics of planar and SPECT/CT bone scan versus ^{18}F-FDG and ^{18}F-sodium fluoride PET/CT scanning. Jpn J Radiol. 2013; 31:766–769. [PubMed: 24085587]

10. Jönsson ÅLM, Simonsen U, Hilberg O, Bendstrup E. Pulmonary alveolar microlithiasis: Two case reports and review of the literature. Eur Respir Rev. 2012; 21:249–256. [PubMed: 22941890]
11. Huqun, Izumi S, Miyazawa H, Ishii K, Uchiyama B, Ishida T, Tanaka S, Tazawa R, Fukuyama S, Tanaka T, Nagai Y, Yokote A, Takahashi H, Fukushima T, Kobayashi K, Chiba H, Nagata M, Sakamoto S, Nakata K, Takebayashi Y, Shimizu Y, Kaneko K, Shimizu M, Kanazawa M, Abe S, Inoue Y, Takenoshita S, Yoshimura K, Kudo K, Tachibana T, Nukiwa T, Hagiwara K. Mutations in the SLC34A2 gene are associated with pulmonary alveolar microlithiasis. Am J Respir Crit Care Med. 2007; 175:263–268. [PubMed: 17095743]
12. Corut A, Senyigit A, Ugur SA, Altin S, Ozcelik U, Calisir H, Yildirim Z, Gocmen A, Tolun A. Mutations in SLC34A2 cause pulmonary alveolar microlithiasis and are possibly associated with testicular microlithiasis. Am J Hum Genet. 2006; 79:650–656. [PubMed: 16960801]
13. Ma T, Ren J, Yin J, Ma Z. A pedigree with pulmonary alveolar microlithiasis: A clinical case report and literature review. Cell Biochem Biophys. 2014; 70:565–572. [PubMed: 24817643]
14. Yin X, Wang H, Wu D, Zhao G, Shao J, Dai Y. SLC34A2 gene mutation of pulmonary alveolar microlithiasis: Report of four cases and review of literatures. Respir Med. 2013; 107:217–222. [PubMed: 23164546]
15. Yang W, Wang Y, Pu Q, Ye S, Ma Q, Ren J, Zhong G, Liu L, Zhu W. Elevated expression of SLC34A2 inhibits the viability and invasion of A549 cells. Mol Med Rep. 2014; 10:1205–1214. [PubMed: 25017204]
16. Hashimoto M, Wang DY, Kamo T, Zhu Y, Tsujiuchi T, Konishi Y, Tanaka M, Sugimura H. Isolation and localization of type IIb Na/Pi cotransporter in the developing rat lung. Am J Pathol. 2000; 157:21–27. [PubMed: 10880371]
17. Forster IC, Hernando N, Biber J, Murer H. Phosphate transporters of the SLC20 and SLC34 families. Mol Aspects Med. 2013; 34:386–395. [PubMed: 23506879]
18. Biber J, Hernando N, Forster I. Phosphate transporters and their function. Annu Rev Physiol. 2013; 75:535–550. [PubMed: 23398154]
19. Nishimura M, Naito S. Tissue-specific mRNA expression profiles of human solute carrier transporter superfamilies. Drug Metab Pharmacokinet. 2008; 23:22–44. [PubMed: 18305372]
20. Murer H, Forster I, Biber J. The sodium phosphate cotransporter family SLC34. Pflugers Arch. 2004; 447:763–767. [PubMed: 12750889]
21. Lederer E. Regulation of serum phosphate. J Physiol. 2014; 592:3985–3995. [PubMed: 24973411]
22. Sabbagh Y, O'Brien SP, Song W, Boulanger JH, Stockmann A, Arbeeny C, Schiavi SC. Intestinal Npt2b plays a major role in phosphate absorption and homeostasis. J Am Soc Nephrol. 2009; 20:2348–2358. [PubMed: 19729436]
23. Sabbagh Y, Schiavi SC. Role of NPT2b in health and chronic kidney disease. Curr Opin Nephrol Hypertens. 2014; 23:377–384. [PubMed: 24848935]
24. Xu H, Bai L, Collins JF, Ghishan FK. Molecular cloning, functional characterization, tissue distribution, and chromosomal localization of a human, small intestinal sodium– phosphate (Na^+–P_i) transporter (SLC34A2). Genomics. 1999; 62:281–284. [PubMed: 10610722]
25. Murer H, Hernando N, Forster I, Biber J. Molecular mechanisms in proximal tubular and small intestinal phosphate reabsorption (Plenary Lecture). Mol Membr Biol. 2001; 18:3–11. [PubMed: 11396609]
26. Murer H, Hildmann B. Transcellular transport of calcium and inorganic phosphate in the small intestinal epithelium. Am J Physiol. 1981; 240:G409–G416. [PubMed: 6264798]
27. Schiavi SC, Tang W, Bracken C, O'Brien SP, Song W, Boulanger J, Ryan S, Phillips L, Liu S, Arbeeny C, Ledbetter S, Sabbagh Y. Npt2b deletion attenuates hyperphosphatemia associated with CKD. J Am Soc Nephrol. 2012; 23:1691–1700. [PubMed: 22859851]
28. Collins JF, Bai L, Ghishan FK. The SLC20 family of proteins: Dual functions as sodium-phosphate cotransporters and viral receptors. Pflugers Arch. 2004; 447:647–652. [PubMed: 12759754]
29. Shannon JM, Hyatt BA. Epithelial-mesenchymal interactions in the developing lung. Annu Rev Physiol. 2004; 66:625–645. [PubMed: 14977416]
30. Warburton D, Schwarz M, Tefft D, Flores-Delgado G, Anderson KD, Cardoso WV. The molecular basis of lung morphogenesis. Mech Dev. 2000; 92:55–81. [PubMed: 10704888]

31. Villa-Bellosta R, Sorribas V. Role of rat sodium/phosphate cotransporters in the cell membrane transport of arsenate. Toxicol Appl Pharmacol. 2008; 232:125–134. [PubMed: 18586044]
32. Andrini O, Ghezzi C, Murer H, Forster IC. The leak mode of type II Na^+-P_i cotransporters. Channels. 2008; 2:346–357. [PubMed: 18989094]
33. Young LR, Borchers MT, Allen HL, Gibbons RS, McCormack FX. Lung-restricted macrophage activation in the pearl mouse model of Hermansky-Pudlak syndrome. J Immunol. 2006; 176:4361–4368. [PubMed: 16547274]
34. Traebert M, Hattenhauer O, Murer H, Kaissling B, Biber J. Expression of type II Na-P_i cotransporter in alveolar type II cells. Am J Physiol. 1999; 277:L868–L873. [PubMed: 10564169]
35. Reimer RJ, Edwards RH. Organic anion transport is the primary function of the SLC17/type I phosphate transporter family. Pflugers Arch. 2004; 447:629–635. [PubMed: 12811560]
36. O'Neill WC. The fallacy of the calcium-phosphorus product. Kidney Int. 2007; 72:792–796. [PubMed: 17609689]
37. Ikegami M. Surfactant catabolism. Respirology. 2006; 11(Suppl. S1):S24–S27. [PubMed: 16423266]
38. Monabati A, Ghayumi M, Kumar PV. Familial pulmonary alveolar microlithiasis diagnosed by bronchoalveolar lavage. A case report. Acta Cytol. 2007; 51:80–82. [PubMed: 17328501]
39. Takahashi H, Chiba H, Shiratori M, Tachibana T, Abe S. Elevated serum surfactant protein A and D in pulmonary alveolar microlithiasis. Respirology. 2006; 11:330–333. [PubMed: 16635094]
40. Pracyk JB, Simonson SG, Young SL, Ghio AJ, Roggli VL, Piantadosi CA. Composition of lung lavage in pulmonary alveolar microlithiasis. Respiration. 1996; 63:254–260. [PubMed: 8815975]
41. Brown J, Mellis CM, Wood RE. Edetate sodium aerosol in Pseudomonas lung infection in cystic fibrosis. Am J Dis Child. 1985; 139:836–839. [PubMed: 3927708]
42. Wang G, Zabner J, Deering C, Launspach J, Shao J, Bodner M, Jolly DJ, Davidson BL, McCray PB Jr. Increasing epithelial junction permeability enhances gene transfer to airway epithelia In vivo. Am J Respir Cell Mol Biol. 2000; 22:129–138. [PubMed: 10657931]
43. Chu Q, St George JA, Lukason M, Cheng SH, Scheule RK, Eastman SJ. EGTA enhancement of adenovirus-mediated gene transfer to mouse tracheal epithelium in vivo. Hum Gene Ther. 2001; 12:455–467. [PubMed: 11268280]
44. Hopkins PM, Kermeen F, Duhig E, Fletcher L, Gradwell J, Whitfield L, Godinez C, Musk M, Chambers D, Gotley D, McNeil K. Oil red O stain of alveolar macrophages is an effective screening test for gastroesophageal reflux disease in lung transplant recipients. J Heart Lung Transplant. 2010; 29:859–864. [PubMed: 20466562]
45. McCormack FX, Gibbons R, Ward SR, Kuzmenko A, Wu H, Deepe GS Jr. Macrophage-independent fungicidal action of the pulmonary collectins. J Biol Chem. 2003; 278:36250–36256. [PubMed: 12857753]
46. Bridges JP, Ludwig MG, Mueller M, Kinzel B, Sato A, Xu Y, Whitsett JA, Ikegami M. Orphan G protein–coupled receptor GPR116 regulates pulmonary surfactant pool size. Am J Respir Cell Mol Biol. 2013; 49:348–357. [PubMed: 23590306]
47. Palaniyar N, Zhang L, Kuzmenko A, Ikegami M, Wan S, Wu H, Korfhagen TR, Whitsett JA, McCormack FX. The role of pulmonary collectin N-terminal domains in surfactant structure, function, and homeostasis in vivo. J Biol Chem. 2002; 277:26971–26979. [PubMed: 12015304]

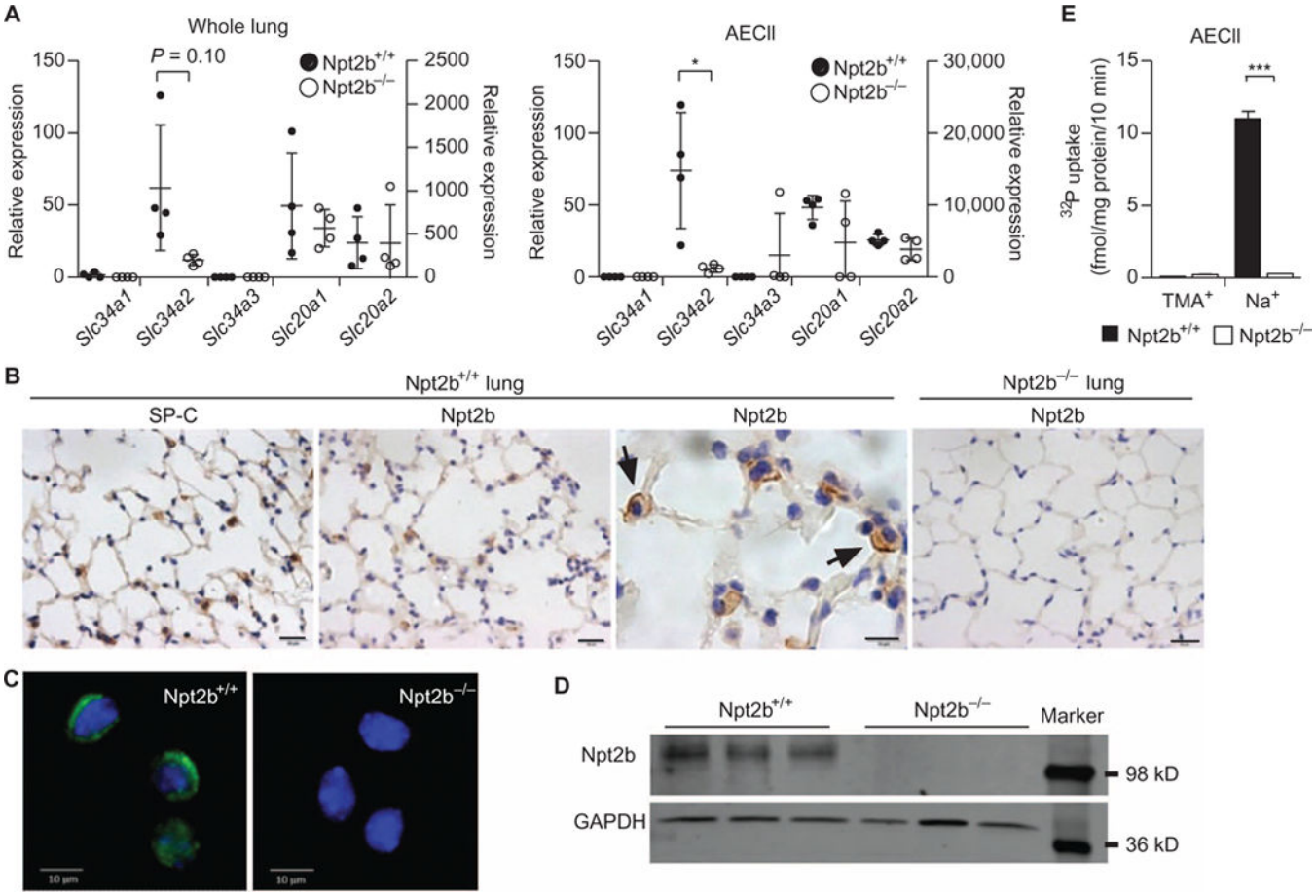

Fig. 1. Deletion of exon 6 of *Slc34a2* results in markedly decreased AECII *Slc34a2* mRNA expression, Npt2b protein expression, and phosphate transport

(**A**) Relative expression of *Slc34* and *Slc20* family phosphate transporters in the whole lung and AECII from 13-week-old Npt2b$^{+/+}$ and Npt2b$^{-/-}$ mice was determined by rtPCR (n = 4 mice per group). The right y axis applies to *Slc34a2*, and the left *y* axis applies to all others. (**B**) Paraffin-embedded lung sections from 13-week-old mice were stained with anti-pro SP-C antibody or anti-Npt2b antibody and observed under light microscopy. Representative images are shown. Arrows demonstrate enhanced Npt2b staining in the apical membrane of AECII. Bold scale bar represents 200, 200, 20, and 200 μm, respectively, from left to right. (**C**) AECII isolated and purified from 13-week-old Npt2b$^{+/+}$ and Npt2b$^{-/-}$ mice were cytospun onto glass slides, reacted with anti-Npt2b antibodies, and stained with diaminobenzidine (DAB) and 4′,6-diamidino-2-phenylindole (DAPI). Representative images are shown. Bold scale bar, 10 μm. (**D**) Immunoblot of Npt2b. Isolated AECII were lysed and loaded at 10 μg of protein per lane onto SDS–polyacrylamide gel electrophoresis (SDS-PAGE) gels. After transfer to polyvinylidene difluoride (PVDF) membrane, a 108-kD band was detected with anti-Npt2b antibody. Anti–glyceraldehyde phosphate dehydrogenase (GAPDH) antibody was used as a loading control. (**E**) ^{32}P uptake into AECII isolated from Npt2b$^{+/+}$ and Npt2b$^{-/-}$ mice was measured in the presence and absence of tetramethylammonium (TMA^{+}) and Na^{+} (n = 3 to 6 mice per group). Data are expressed as

means ± SD. *$P < 0.05$, ***$P < 0.001$; exact P values can be found in table S2 (unpaired t test with Welch correction).

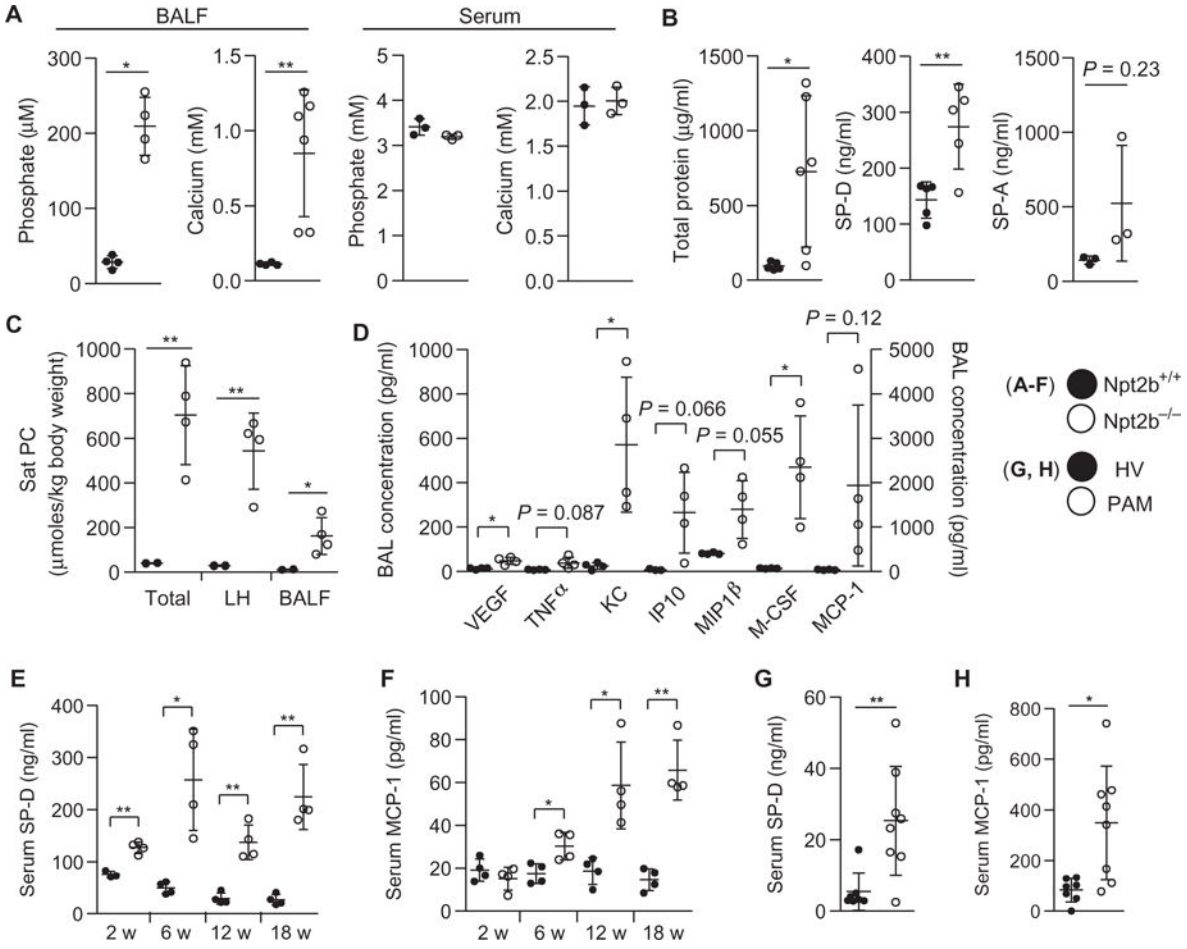

Fig. 2. Deletion of Npt2b in the lung epithelium results in altered alveolar homeostasis

(**A** to **H**) Alveolar and serum concentrations of markers of alveolar homeostasis from Npt2b$^{+/+}$ (closed circles) (A to F) and Npt2b$^{-/-}$ mice (open circles) (A to F), healthy volunteers (HV) (closed circles) (G and H), and PAM patients (open circles) (G and H). (A) The phosphate and calcium concentrations in BALF and serum were measured by colorimetric assay (n = 3 to 6 mice per group). (B) Total protein in BALF was measured using bicinchoninic acid (n = 5 to 6 mice per group), and mouse SP-D and SP-A in BALF were quantified by enzyme-linked immunosorbent assay (ELISA) (n = 3 to 5 mice per group). (C) Sat PC was measured in lung homogenates (LH) and BALF of 12- to 14-week-old Npt2b$^{+/+}$ and Npt2b$^{-/-}$ mice (n = 4 mice per group). (D) Luminex cytokine array of BALF (n = 4 mice per group). The right y axis applies to MCP-1, and the left y axis applies to all other cytokines. (E and F) Serum SP-D and MCP-1 from mice were measured by ELISA at the indicated ages [in weeks (w)] (n = 4 mice per group). (G and H) Human SP-D and MCP-1 in the serum from healthy volunteers and PAM patients were examined by ELISA (n = 7 to 8 per group). Data are expressed as means ± SD. *P < 0.05, **P < 0.01; exact P values can be found in table S2 (unpaired t test with Welch correction).

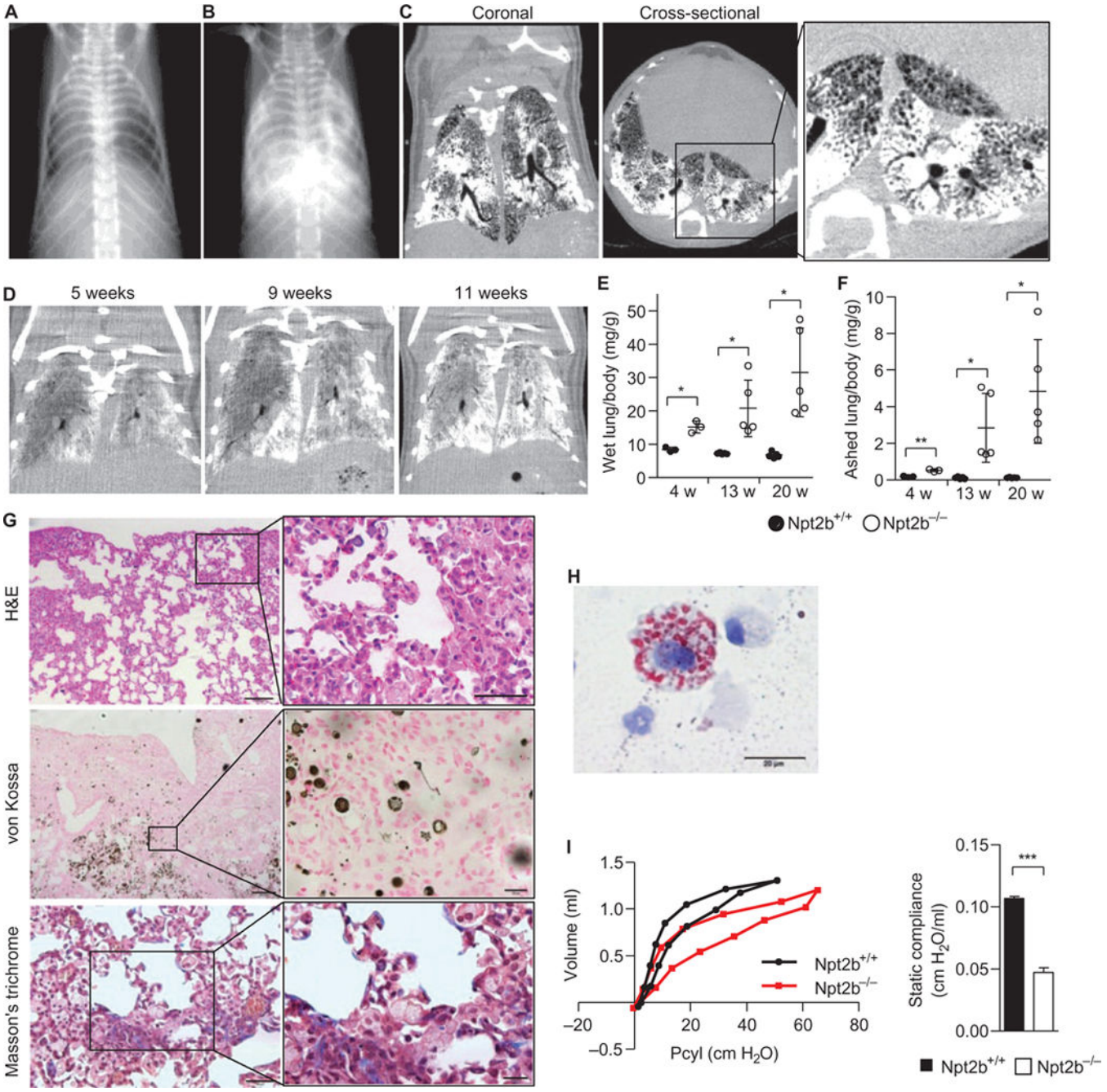

Fig. 3. Radiographic, histologic, and physiologic consequences of Npt2b deletion in mice

(**A** and **B**) Radiograph of Npt2b$^{+/+}$ (A) and Npt2b$^{-/-}$ (B) mice, revealing dense opacities, consistent with extensive calcium deposition. (**C**) Coronal and cross-sectional CTs of Npt2b$^{-/-}$ mice demonstrating diffuse opacities, with areas of focal hyperdense calcium deposition containing air bronchograms. Window level, −150 HU; window width, 1500 HU. (**D**) Representative coronal CT cuts of a single Npt2b$^{-/-}$ mouse serially imaged at 5, 9, and 11 weeks. (**E** and **F**) Wet (E) and ashed (F) lung weights of Npt2b$^{+/+}$ and Npt2b$^{-/-}$ mice normalized to body weight at the indicated ages (n = 3 to 5 mice per group). (G) Paraffin-embedded lung sections from 16-week-old Npt2b$^{-/-}$ mice were stained with hematoxylin

and eosin (H&E), von Kossa reagent, and Masson's trichrome reagent. BAL cells from Npt2b$^{-/-}$ mice were cytospun onto glass slides and stained with Oil Red O reagent. Representative images are shown. Bold scale bars on low- and high-power images, respectively, are 100 and 50 μm for H&E, 200 and 20 μm for von Kossa, and 50 and 20 μm for Masson's trichrome. (**H**) On the cytospun specimen, the bold scale bar is 20 μm. (I) The pressure/volume and compliance measurements were made using the forced oscillation method. Pcyl refers to "pressure in the cylinder." Data are plotted as described in Materials and Methods (mean, 26 versus 37 μl/cm H_2O/ml total lung capacity from Npt2b$^{+/+}$ and Npt2b$^{-/-}$ mice, respectively; $n = 3$ mice per group). Data are expressed as means ± SD. *$P < 0.05$, **$P < 0.01$, and ***$P < 0.001$; exact P values can be found in table S2 (unpaired t test with Welch correction).

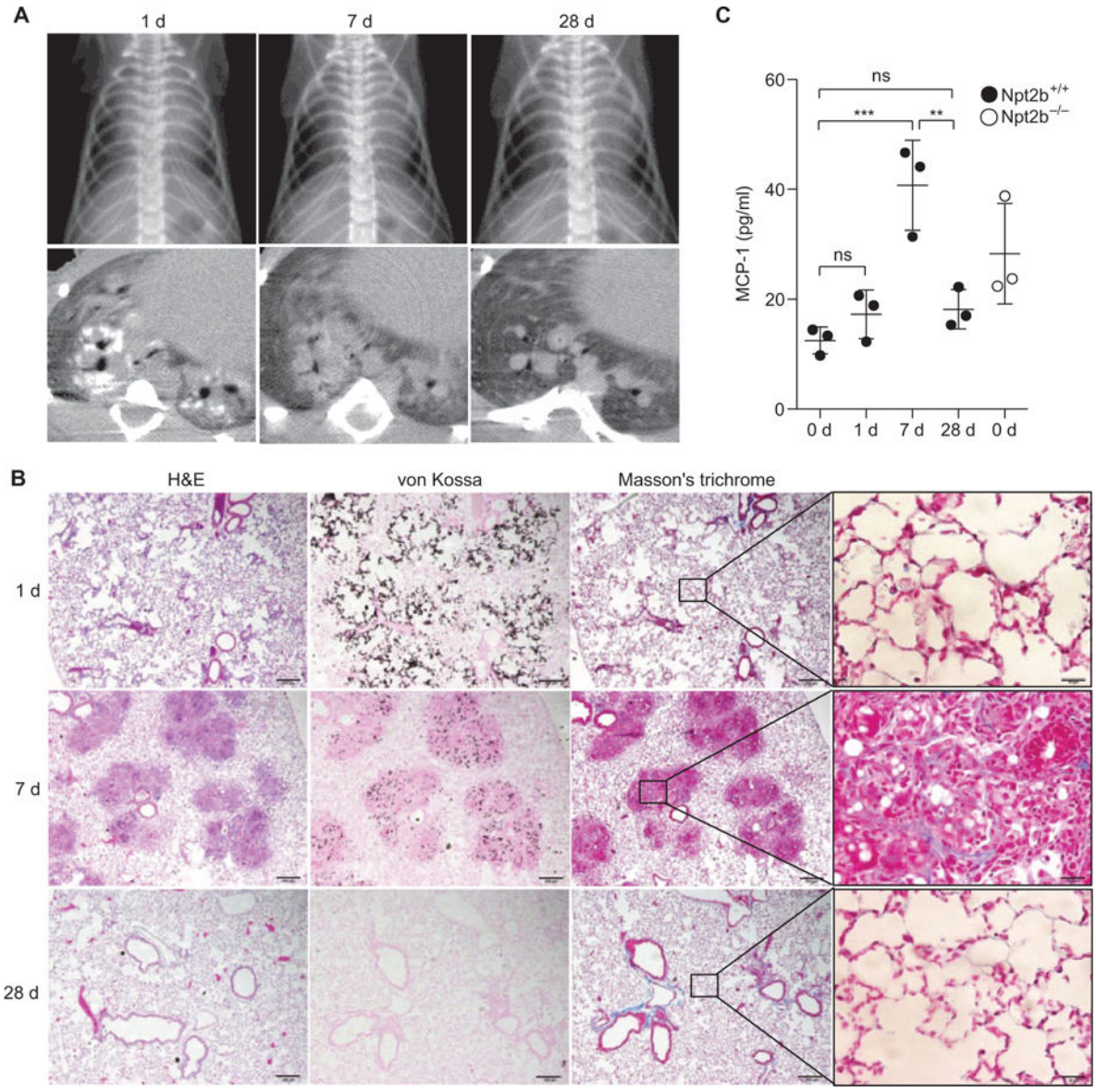

Fig. 4. Adoptive transfer of microliths induces transient alveolar inflammation

(**A**) Microliths isolated from the lungs of Npt2b$^{-/-}$ mice were instilled into the lungs of Npt2b$^{+/+}$ mice. Serial radiographs and microCT images were taken. (**B**) Mice were sacrificed at the indicated times in days (d) after instillation, and the lungs were fixed and stained with H&E, von Kossa reagent, and Masson's trichrome reagent as indicated. Representative images are shown. Bold scale bar, 200 μm (low magnification) and 20 μm (high magnification). (**C**) Serum MCP-1 from Npt2b$^{+/+}$ mice after adoptive microlith transfer (closed circles) and 16-week-old Npt2b$^{-/-}$ mice (open circles, for comparison) were measured by ELISA (n = 3 mice per group). Data are expressed as means ± SD. $^{**}P < 0.01$, $^{***}P < 0.001$; ns, not significant; statistical analysis can be found in table S2 [analysis of variance (ANOVA)].

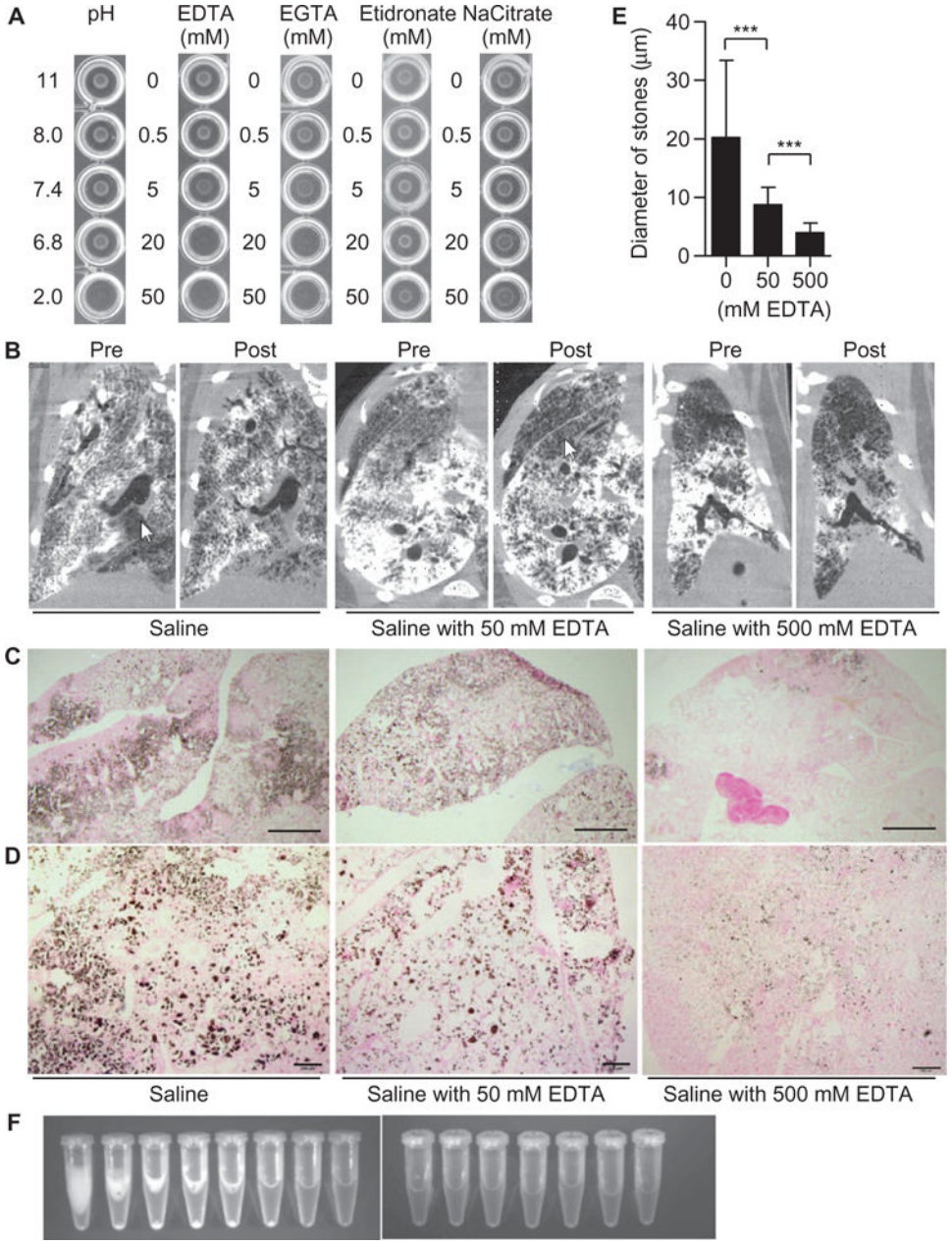

Fig. 5. Postmortem therapeutic EDTA lavage reduce microlith burden

(**A**) Microliths were isolated from Npt2b$^{-/-}$ mice by lavage and incubated with solutions containing various chelating agents or levels of acidity. The mixtures were plated in round-bottom plates and centrifuged. (**B**) MicroCT imaging before and after repeated BAL (1 ml, 15 cycles) of postmortem Npt2b$^{-/-}$ mice with 0, 50, or 500 mM EDTA. (**C** and **D**) Lung sections from lavaged mice were stained with von Kossa reagent and viewed under low (C) and high magnifications (D). Bold bar represents 2 (C) and 200 mm (D). (**E**) The diameter of residual crystals on post-lavage lung histology was measured under the microscope. Data are expressed as means ± SD from at least 50 stones per high-powered field. ***$P < 0.001$; statistical analysis can be found in table S2 (ANOVA). (**F**) Recovered BALF from

sequential instillation/aspiration cycles of 500 mM EDTA is shown (left to right, cycles 1 to 15, respectively). Note the foamy appearance of the first five tubes consistent with excess surfactant material, as well as pelleted microliths in the first six to seven tubes.

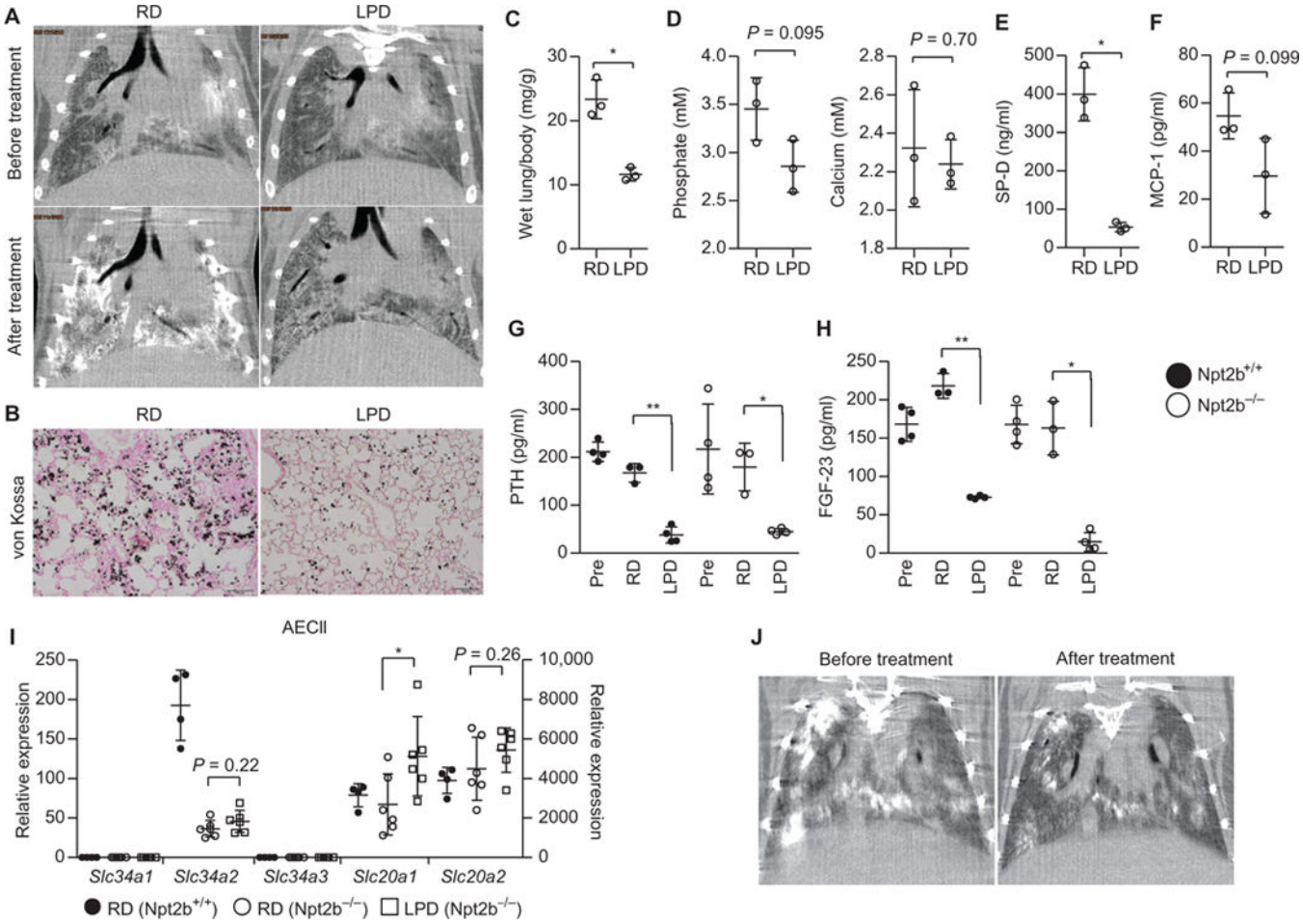

Fig. 6. LPD prevents and improves microlith accumulation

(**A**) MicroCT imaging before and after challenging 3-week-old mice with RD or LPD for 2 months. (**B**) von Kossa staining was performed after dietary challenge. Representative specimens are shown. Bold scale bars, 100 μm. (**C**) Wet lung weights of mice normalized to the body weight from RD and LPD groups (n = 3 mice per group). (**D** to **F**) Phosphate, calcium (D), SP-D (E), and MCP-1 (F) in serum from RD and LPD group mice were measured as indicated in Materials and Methods (n = 3 mice per group). (**G** and **H**) FGF-23 (G) and PTH (H) in serum from mice fed with RD or LPD for 2 weeks were measured as indicated in Materials and Methods. The serum from pretreated mice were used for the comparison (Pre) (n = 3 to 4 mice per group). (**I**) Relative expression of *Slc34* and *Slc20* family phosphate transporters in the AECII from Npt2b$^{+/+}$ mice treated with RD (closed bar) and Npt2b$^{-/-}$ mice treated with RD (ash color bar) or LPD (open bar) for 2 weeks were determined by rtPCR (n = 4 to 6 mice per group). The right axis applies to *Slc34a2*, and the left y axis applies to all others. (**J**) Mice (25 to 28 weeks old) were fed with LPD for 4 weeks and evaluated by pre- and post-microCT. Data are expressed as means ± SD. *P < 0.05, **P < 0.01; exact P values can be found in table S2 (unpaired t test with Welch correction).